

Effect of non-parallel applicator insertion on microwave ablation zone size and shape

by

Austin White

B.S., Kansas State University, 2016

A THESIS

submitted in partial fulfillment of the requirements for the degree

MASTER OF SCIENCE

Department of Electrical Engineering  
College of Engineering

KANSAS STATE UNIVERSITY  
Manhattan, Kansas

2018

Approved by:

Major Professor  
Dr. Punit Prakash

# Copyright

© Austin White 2018

## Abstract

Microwave ablation is clinically used to thermally ablate cancerous tissue in the liver and other organs. When treating large tumor volumes, physicians may use multiple antennas simultaneously. Multiple antennas can ablate a larger tissue volume while using the same total power as a single antenna. Pre-clinical simulation and experimental studies most often presume parallel insertion of antennas. However, due to anatomical constraints, such as the presence of ribs and the diaphragm, it is often challenging to insert antennas in a parallel fashion in practice. Previous studies have attempted to analyze the effect of non-parallel antenna insertion on ablation outcome using computational and experimental approaches; however, they were limited because they did not account for dynamic temperature-dependent changes in tissue electrical properties in simulations and employed limited experimental validation. In this thesis, we have developed improved models of multiple-antenna microwave ablation, including accounting for the effects of temperature-dependent changes in tissue properties. We have also developed a system for experimental assessment of ablation zone profiles in *ex vivo* tissues. By utilizing 3D printing, we have constructed a device to precisely position antennas within experimental tissue samples and allows for accurate sectioning of the ablation zone relative to the plane of antenna insertion. Furthermore, we implemented image processing techniques for quantifying the size and shape of experimental ablation zones. This enables more accurate and repeatable comparisons of ablation profiles between simulations and experiments. We found that for an inter-antenna spacing in the range of 10 – 20 mm, simulations and experiments indicated that the ablation zone volumes may change by up to 30% due to non-parallel antenna insertion.

# Table of Contents

List of Figures .....	v
List of Tables .....	vii
Chapter 1 - Introduction.....	1
Techniques for inducing ablation .....	2
Clinical experience with current ablation modalities .....	5
Multiple antenna ablation .....	6
Chapter 2 - Methods.....	9
Computation simulation.....	9
Experimental validation.....	15
Area comparison with Dice Similarity Coefficient (DSC).....	26
Chapter 3 - Results.....	28
Experimental.....	28
Simulation.....	32
Extended Simulated Results .....	36
Chapter 4 - Discussion .....	38
Chapter 5 - Conclusion .....	40
References.....	41

## List of Figures

Figure 1: Block diagram of typical ablation system .....	2
Figure 2: Alignment of polar water molecules with the orientation of the applied electric field. Adapted from [24], [25]. .....	4
Figure 3: Electric field radiation pattern for standard dipole.....	5
Figure 4: Large tumor with multiple ablations for removal. Adapted from [32] .....	7
Figure 5: Example ablation zone extents as reported from an ablation device manufacturer. Adapted from [33].....	7
Figure 6: Computation Steps COMSOL takes during simulation .....	9
Figure 7: Simulation setup as seen at the XZ plane. blue is the liver and .....	11
Figure 8: Model with tetrahedral mesh shown. ....	14
Figure 9: Liver ablation base in white, note the slicing groove down the sides. The blue block (template block) held the antennas in position for the indicated ablation. The 20->20 figures on the template block indicates a $D_{ins}$ distance is 20mm and a $D_{tip}$ distance of 20mm repectively. ....	15
Figure 10: $S_{11}$ plot from two of the dipole antennas built.....	17
Figure 11: Left- Antennas without the Teflon coating .....	17
Figure 12: Setup for experimental validation. ....	18
Figure 13: Scanned Image of a 20 mm Parallel Ablation.....	19
Figure 14: Color spaces used in ablation detection after threshold. ....	21
Figure 15: Combined color spaced image with Gaussian blur applied .....	22
Figure 16: Image after morphological operators. ....	22
Figure 17: All holes filled.....	23

Figure 18: Largest area in picture .....	24
Figure 19: Outline of ablation Area .....	24
Figure 20: Ablation with the centroid shown at the pink dot. ....	25
Figure 21: Aligned and Rotated Ablation Shapes for 20mm Parallel Ablation (colors are inverted, 0 is white).....	26
Figure 22: Ablations all resulted in a shape in between the shown red and green lines for a given scenario. Lines that are close together imply a smaller uncertainty for that ablation zone. .	30
Figure 23: 75% contours of ablations for each scenario. This is what a typical ablation might look like for the antenna spacing, insertion angle, and power.....	31
Figure 24: Area of ablation comparing parallel to on parallel in experimentation. The contours shown are the 75% confidence contours.....	32
Figure 25: Simulation 55 °C XZ isothermal contours. ....	33
Figure 26: Simulation 55 °C YZ isothermal contours .....	34
Figure 27: Simulation 55 °C XY isothermal contours.....	35
Figure 28: Overlaid 55°C isothermal outline of parallel and non-parallel cases.....	36

## List of Tables

Table 1: Data for estimating ablation zone size following 10 min, 45 W MWA. Data taken from [33]. The variables S, A, B, C, and M are illustrated in Figure 5. ....	7
Table 2: Dimensions of simulation illustrated in Figure 7 .....	11
Table 3: Constants used in the calculations for dynamically changing liver properties.....	13
Table 4: Mesh parameters used in simulation.....	13
Table 5: Table showing the DSC of the experimental ablation zone for antennas inserted in the parallel case compared to the non-parallel case.....	29
Table 6: DSC of simulation comparing ablation area of the parallel case to the corresponding non-parallel case (i.e. 15mm to 15->10) in the XZ plane. ....	37
Table 7: Volumetric DSC for simulations with 20 mm antenna spacing .....	37
Table 8: Volumetric DSC for simulations with 15 mm antenna spacing .....	37
Table 9: Volumetric DSC for simulations with 10 mm antenna spacing .....	37

## Chapter 1 - Introduction

Liver cancer is a significant global health problem. There are over 700,000 fatalities attributed to it annually, with about 30,000 in the United States of America alone [1], [2]. Primary liver cancer, hepatocellular carcinoma (HCC), accounts for over 85% of these cases [1]. The liver is also the most frequent organ to have metastatic cancer growth (cancer that originated in another organ but has spread) [3]. Without treatment, median survival of patients with liver cancer is only 1.6 months [4].

The current gold standard treatment options for HCC are either liver transplantation or surgical removal of the tumor. In the case of surgical removal of a tumor, doctors also remove a small margin (3-5 mm) of healthy tissue to assure complete removal of all cancerous cells from the liver. Unfortunately, many patients are not eligible for either liver transplant or surgical resection; in fact, only about 20% of patients with HCC are eligible to undergo surgical resection [5]–[7]. This may be due to the tumor being located in a technically challenging anatomical region, or other factors such as medical comorbidities that make surgery more risky [8]. Thus, a majority of patients with HCC are in need of alternate methods for treating cancerous tissue [9].

Ablative therapies are emerging as a viable treatment option for localized tumors [10]. In this context, the term ablation refers to the destruction of cells by heat, usually in excess of 50 °C for a few minutes [11]. Ablation has several advantages over a traditional resection, the primary advantage being that surgical resection is inherently a highly invasive procedure and has a relatively high risk of complications compared to local ablative therapies [7], [12], [13]. Percutaneous ablation has overall lower morbidity and mortality rate as compared to surgical resection [7], [14]. Ablation techniques that have been employed in clinical use include lasers,

ultrasound, radio frequency currents, and microwaves [15]–[17]. Percutaneous ethanol injection has also been employed as a non-thermal ablative modality.

Figure 1 illustrates the major components a typical thermal ablation system. An applicator is inserted into the patient, typically under image guidance, to ensure an accurate probe placement. The microwave power source delivers microwaves to the applicator which then is radiated into the treatment site in the patient. Some ablation systems employ feedback to guide the adjustment of power delivery parameters during the procedure.

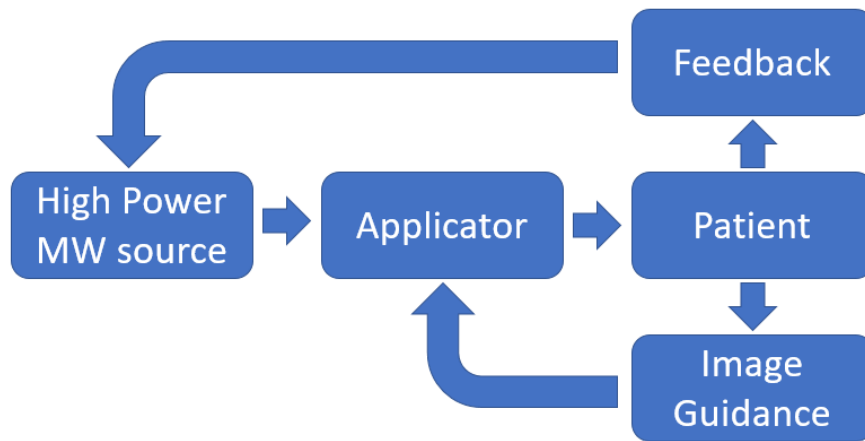


**Figure 1: Block diagram of typical ablation system**

### **Techniques for inducing ablation**

Radiofrequency ablation (RFA) is the most commonly used ablative technique and has been shown to be clinically effective for treating small tumors (< 3 cm) [1], [18], [19]. The principal method of heat deposition in tissue during RFA is through the Joule effect (resistive losses in the tissue that cause heating) from ionic currents through the body [19], [20]. The ionic current that flows through the tissue is induced by the applicator, which is called an RF ablation probe or electrode. The typical operating frequency for RF ablation systems is usually around 460

kHz [18]. RFA systems employ a minimally invasive probe (typically, < 3 mm diameter) inserted percutaneously into the tissue and a large dispersive ground pad placed farther away on the body. Ionic currents flow in between the inserted probe and the grounding pad. If the grounding pad is sufficiently large, then the current density will be low enough that tissue heating will be kept to a minimum near the grounding pad, instead it will be predominantly centered around the active RFA probe.

A challenge with RFA is that only the tissue near the probe (~few mm) is heated directly with the induced RF current. The ablation zone further grows as a result of the thermal conduction of heat, flowing from the warmer parts of the tissue to the cooler parts [18]. Because thermal conduction is the passive transfer of heat, and the heat is not directed by the applicator, the ablation zone is largely based on the blood perfusion around the applicator. If the tumor is near a large blood vessel, the blood flow will act as a large heatsink. This may result in inadequate heating of the targeted tissue to achieve cell death [21].

Microwave ablation (MWA) emerged in the 1990s and has been slowly growing in clinical use for ablation of large targets in vascular organs (e.g. liver tumors) due to the many advantages that it has over RFA [7]. The ability to treat larger tumors, not requiring grounding pads, and not being as susceptible to the heat sink effect as RFA, are the principle advantages of MWA [22], [23]. For RFA, the ablation zone primarily grows passively via thermal conduction, whereas in MWA the ablation zone is primarily determined by the radiated electromagnetic wave being absorbed by surrounding tissue. Similar to an RF ablation system, MWA also requires a small probe that is inserted in to the treatment area. This probe is typically about the same length and diameter as the RF probe and is fed by a signal generator, although the MWA signal generator is operating at a much higher frequency, typically at either 915 MHz or 2.45 GHz. The MWA probe

radiates a time-varying electromagnetic field into the surrounding tissue. As the electromagnetic wave propagates, the electric field forces water and other polar molecules to align with the applied electric field. This rotational movement of the polar molecules leads to heating (see Figure 2).

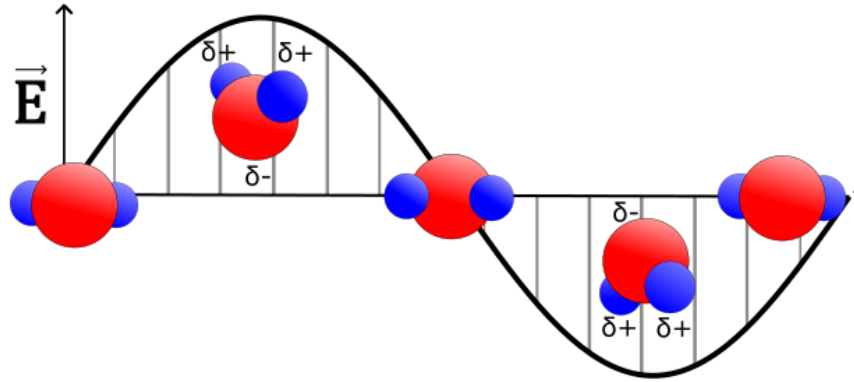


**Figure 2: Alignment of polar water molecules with the orientation of the applied electric field. Adapted from [24], [25].**

Tissue dielectric properties determine the penetration depth of the electromagnetic wave. Considering the propagating electromagnetic wave as a plane wave traveling through a lossy medium, as shown in Equation 1, can be instructive, although it is noted that the tissue surrounding the antenna is in the antenna's near-field, and thus plane wave conditions may not hold. In this equation,  $\alpha$  is the attenuation constant and is determined by the dielectric properties of the material within which the electromagnetic wave is traveling. Equation 1 shows that the electric field intensity in a lossy material, such as tissue, decays exponentially.

$$\mathbf{E}(z, t) = E_0 e^{-\alpha z} \cos(\omega t - \beta z) \mathbf{a}_z \quad (1)$$

Since the electric field from the MW antenna is the primary factor that determines the shape of the ablation, careful design of the antenna is important in shaping the ablation. In this study the

microwave antenna used was a dipole antenna. The radiation pattern is symmetric across the angular expanses, as seen in Figure 3.

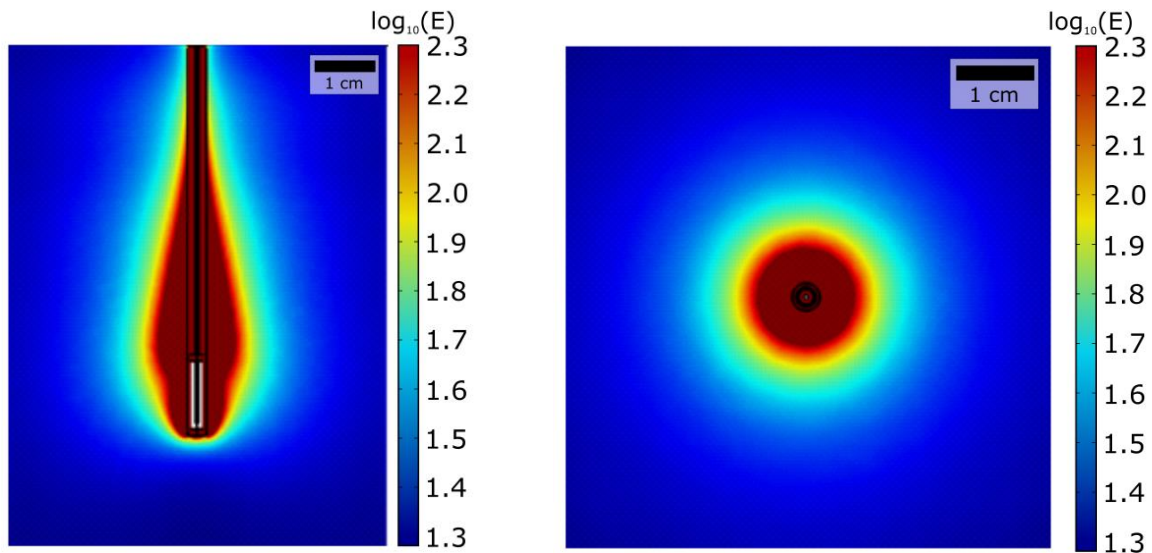


**Figure 3: Electric field radiation pattern for standard dipole.**

Some other ablation modalities include Percutaneous Ethanol Injection (PEI), ultrasound, and lasers. PEI is a method of ablation that uses alcohol injections to kill the cancerous cells. Laser ablation system employ fiber-optic devices inserted into the cancer nodule in order to induce heating with light [18]. Ultrasound uses pressure waves to induce heating and has multiple transducers along the probe length, which can be used to control the heating along the length of the applicator [26].

### **Clinical experience with current ablation modalities**

A large fraction of patients with liver tumors are ineligible for surgical resection because of their health status or location of the tumor. For these cases, alternative treatments, such as ablation may be employed. It has been found that surgical resection of HCC has a 5-year survival

of about 50% [27], [28]. However, if there are multiple tumors in the liver, then resection is not always recommended [27], [29].

RFA is a viable minimally-invasive alternative for patients that are ineligible for surgical resection. Recent studies have shown that the 5-year survival rates for RFA can be higher than both traditional surgical resection and PEI, for small tumors, with a survival rate of up to 60% [28], [29]. Early clinical studies using MWA suggest 5-year survival rate ranging from about 30% to 70% [30].

### **Multiple antenna ablation**

For treating large tumors, multiple ablations may be necessary in order to cover a sufficient volume, as depicted in Figure 4. From this figure, it is clear, that since a probe can only ablate tissue over a limited distance, it may not cover enough volume to assure complete destruction of a large tumor and a safety margin. In this case, it would take multiple separate ablations to complete the operation.

Physicians may accomplish this by employing multiple antennas simultaneously. The physician would insert the required number of antennas based on the size of the tumor and the anticipated extent of the ablation zone. An example of ablation zone profile data provided by ablation device vendors can be seen in Table 1. Looking at this and Figure 5, one can see how a physician might use this information to estimate a potential ablation size for a given antenna configuration, applied power, and duration of ablation.

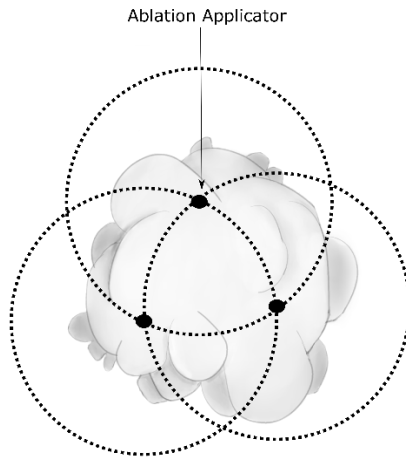


**Figure 4: Large tumor with multiple ablations for removal. Adapted from [32]**

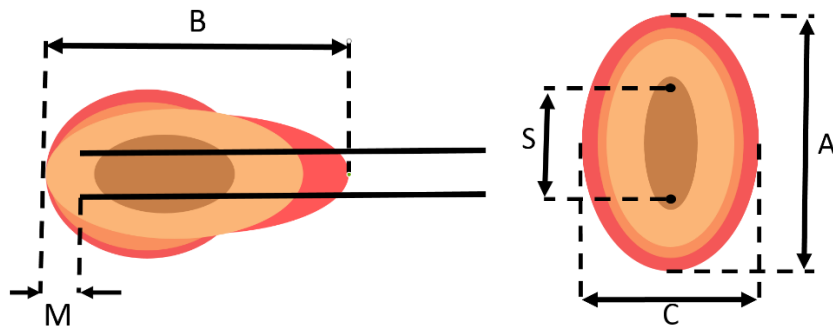


**Figure 5: Example ablation zone extents as reported from an ablation device manufacturer. Adapted from [33]**

S	1.5 cm	2.0 cm
A	3.9 cm	4.4 cm
B	4.7 cm	4.5 cm
C	3.0 cm	3.1 cm
M	0.6 cm	0.6 cm
Volume	29 cm <sup>3</sup>	32 cm <sup>3</sup>

**Table 1: Data for estimating ablation zone size following 10 min, 45 W MWA. Data taken from [33]. The variables S, A, B, C, and M are illustrated in Figure 5.**

As one might notice from the manufacturer's guidelines in Figure 5, the indicated ablation zone was calculated given with the assumption that the antennas are inserted in a parallel fashion. Unfortunately, parallel insertion of antennas may not always be feasible [34]. One of the primary obstructions would be a bone or an organ that is in the insertion path or near the ablation zone. Another issue that could cause this is that the antennas may diverge from a straight path upon insertion due to the mechanical properties of the antenna and tissue.

Assuming linearity, the total electric field profile in tissue can be estimated as the superposition of the electric fields due to each antenna. Thus, the position of the antennas relative to each other may considerably impact the total electric field, which will in turn impact the power absorption and tissue heating profiles. Other studies have investigated this question of how non-parallel insertion of multiple antennas can influence the ablation volume. Mukherjee employed simulations and experiments in *ex vivo* tissue to assess the impact of non-parallel insertion on microwave ablation patterns with dipole antennas operating at 915 MHz and 2.45 GHz [34]. While that study concluded that the difference between parallel and non-parallel ablations was larger for 915 MHz, a limitation of the study was that simulations did not consider dynamic temperature-dependent changes in tissue electrical properties. Further, only a limited set of experimental measurements were conducted.

The objective of this thesis is to determine how ablation zones created with 2.45 GHz dipole antennas inserted in a non-parallel manner compare to ablation zones when the antennas are inserted in a parallel manner. Multi-physics computational models of microwave ablation and experiments in *ex vivo* liver tissue were employed for this analysis. Image processing techniques were employed to outline experimental ablation zone profiles for comparison against simulated profiles.

## Chapter 2 - Methods

### Computation simulation

Multi-physics computational models of microwave tissue heating were implemented with COMSOL Multiphysics (v5.2a). COMSOL models use the Finite Element Method (FEM); a method that discretizes the materials in the model into elemental shapes. The numerical quantities (temperature and electric field) are calculated at the vertices of these shapes, called mesh points. Models were employed to compute the electric fields radiated into tissue, and the subsequent heat transfer due to absorbed microwave power. Figure 6 illustrates the coupling between the electromagnetic and heat transfer simulations employed in this thesis.

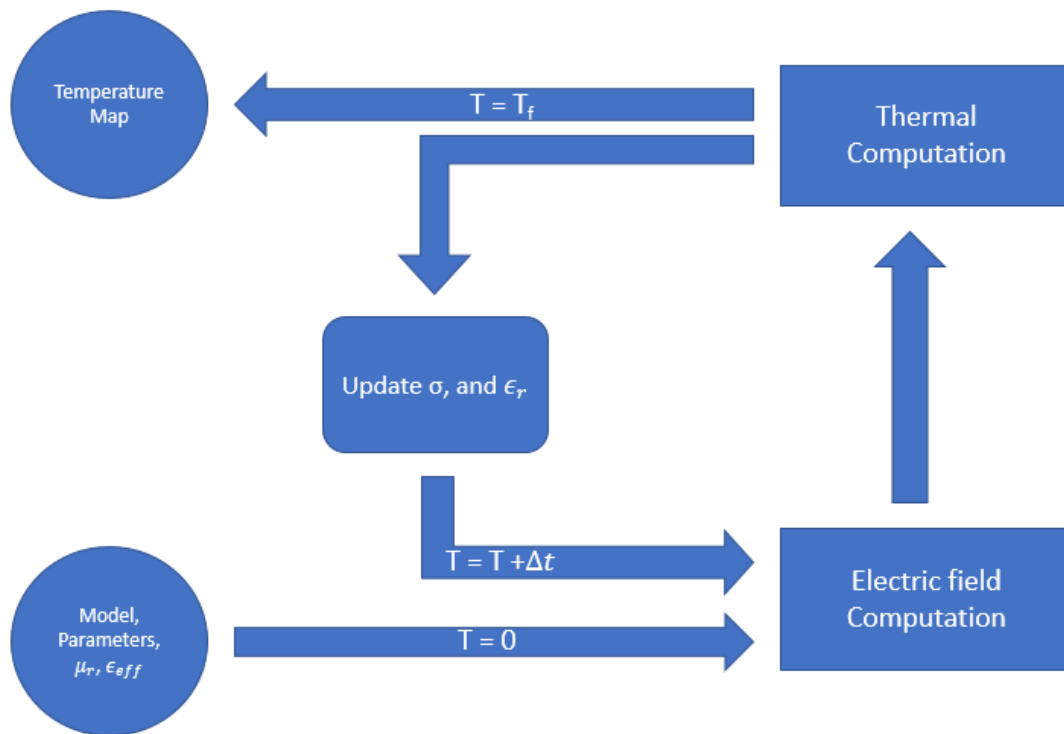


**Figure 6: Computation Steps COMSOL takes during simulation**

The model liver had a width and depth of 60 mm and a height of 80 mm. These dimensions were selected because it was the largest we were able to consistently retrieve for the experimental

validation without large vessels and other inhomogeneities. The simulation model contained two antennas which were designed to be operated at 2.45 GHz (specifications given by Curto et al [17]). The antennas had 15 W of power applied to them (power measured at the antenna input, not the generator). We chose this power to be as close as possible to be clinically relevant, while yielding ablation zone sizes not impacted by the limited size of the tissue samples used in experiment.

We simulated a total of nine different antenna insertion configurations. There were three parallel cases and six non-parallel cases. The parallel cases had antennas inserted into the liver with the center of the coax at the distance  $D_{\text{ins}}$  away from each other. The non-parallel cases had the tip of each antenna moved toward the center line by 2.5 mm, 5 mm, or 7.5 mm each, resulting in the tips being either 5 mm, 10 mm, or 15 mm away from each other. A diagram showing the setup is below in Figure 7, along with Table 2 which contains a list of all scenarios and corresponding measurements.

$D_{\text{ins}}$  is the nominal distance between the antennas.  $D_{\text{tip}}$ , the tip distance, is the distance between the tips of the antennas. For any parallel case,  $D_{\text{ins}}$  is equal to  $D_{\text{tip}}$ . For the non-parallel cases,  $D_{\text{tip}}$  was changed in multiples of 5 mm (each antenna moved 2.5 mm). The tip of each antenna was moved inward by half the total tip displacement, so the setup was always symmetric down the center line.  $L_{\text{ins}}$  is the distance between the tip of the antenna and the top of the liver. It is the same length as the length of an antenna inserted into the liver for a parallel case. The total length of the antenna in the liver slightly increases for a nonparallel case in order to maintain the same tip depth from the surface of the liver. The depth of the antennas tip from the top of the liver remained constant in all scenarios.  $L_l$  was chosen by us to act as a reference to define the

insertion distance. As illustrated in Figure 7, ablation zone extents were assessed in primarily the XZ plane.

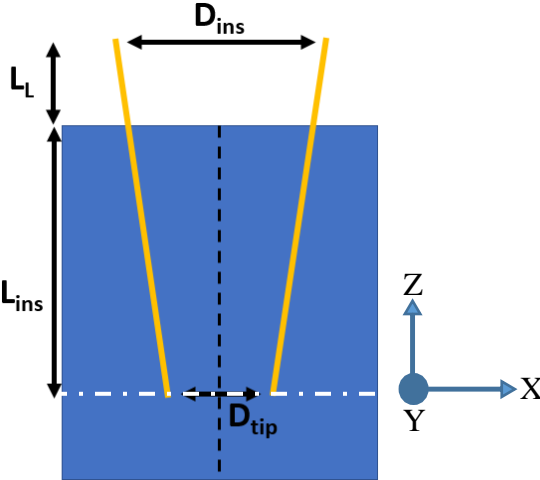


**Figure 7: Simulation setup as seen at the XZ plane. blue is the liver and yellow bars are the antennas.**

Setup Dimensions	$D_{tip}$	$D_{ins}$	$L_{ins}$	$L_L$
20 mm Parallel	20 mm	20 mm	60 mm	48 mm
20 mm to 15 mm	15 mm			
20 mm to 10 mm	10 mm			
20 mm to 5 mm	5 mm			
15 mm Parallel	15 mm	15 mm		
15 mm to 10 mm	10 mm			
15 mm to 5 mm	5 mm			
10 mm Parallel	10 mm	10 mm		
10 mm to 5mm	5 mm			

**Table 2: Dimensions of simulation illustrated in Figure 7**

Equation 2 was used to calculate the electric field at all mesh points. Here  $\mu_r$  is the relative permeability,  $\epsilon_r$  is the relative permittivity and  $\sigma$  is the electrical conductivity of our material.  $c_0$  is the speed of light in free space,  $\omega = 2\pi f$ , and  $\mathbf{E}$  is the vector with x, y, and z components ( $\frac{V}{m}$ ). From the electric field we can calculate how much energy is absorbed in the tissue.

$$\nabla \times (\mu_r^{-1} \nabla \times \mathbf{E}) - \frac{\omega^2}{c_0^2} \left( \epsilon_r - \frac{i\sigma}{\omega\epsilon_0} \right) \mathbf{E} = 0 \quad (2)$$

To calculate how much heat is produced from the electric field, the heat equation as seen in Equation 3 below was used. In this equation, T is the temperature (K),  $\rho$  is the liver density ( $\frac{kg}{m^3}$ ), and C is the specific heat capacity of tissue ( $\frac{J}{kg \cdot K}$ ).  $Q_e$  is the time-averaged electromagnetic power density in tissue ( $\frac{W}{m^3}$ ).  $Q_e$  is calculated from Equation 4 where  $\sigma$  is in  $\frac{S}{m}$ . We did not include blood perfusion in our simulation as our *ex vivo* experimentation would also lack blood perfusion and the primary goal of this work was to compare simulation results with experimental measurements.

$$\rho C \frac{\partial T}{\partial t} = \nabla \cdot k \nabla T + Q_e \quad (3)$$

$$Q_e = \frac{1}{2} \sigma |\mathbf{E}|^2 \quad (4)$$

The electrical properties of liver tissue at 2.45 GHz were dynamically adjusted as a function of the temperature of the liver. The functions we used were defined by Ji and Brace [35]:

$$\epsilon_r(T) = a_3 \left\{ 1 - \frac{1}{1 + \exp[a_1(a_2 - T)]} \right\} + 1 \quad (5)$$

$$\sigma(T) = a_3 \left\{ 1 - \frac{1}{1 + \exp[a_1(a_2 - T)]} \right\} \quad (6)$$

Where  $a_1, a_2, a_3$  in equations 5 and 6 are defined as listed in Table 3. These are directly from [35] with the exception of  $a_3$ . This parameter was slightly modified so that the dielectric

properties of the liver,  $\sigma$  and  $\epsilon$ , would match those given by Hasgall *et al.* in the tissue properties database at 20°C [36].

Regression Coefficients	$a_1$	$a_2$	$a_3$
$\epsilon_r$	0.0764	82.271	43
$\sigma$	0.0697	85.375	1.75

**Table 3: Constants used in the calculations for dynamically changing liver properties**

The mesh for the simulation was a tetrahedral, the parameters that COMSOL used to generate the mesh are shown below in Table 4. The copper in the antennas was modeled as a perfect electric conductor. An illustration of the model with the tetrahedral mesh COMSOL generated is shown in Figure 8. The heterogeneity of the mesh was selected as a balance between accuracy and computational burden.

	Liver	Port	Teflon
Max element size (mm)	5	.1	.5
Min element size (mm)	10.8	10.8	10.8
Max growth rate	1.5	1.1	1.5
Curvature Factor	.6	.6	.6
Resolution of narrow regions	.5	.5	.5

**Table 4: Mesh parameters used in simulation**

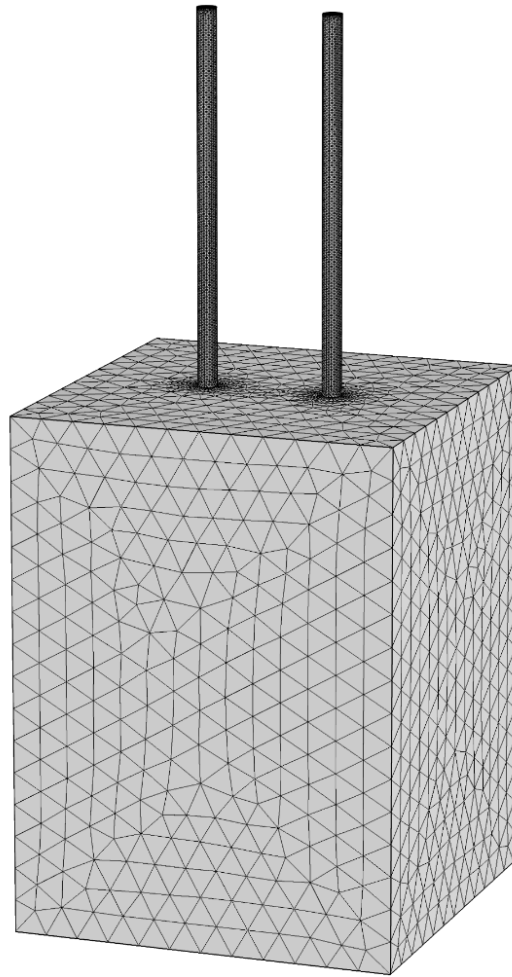


**Figure 8: Model with tetrahedral mesh shown.**

An electrical scattering boundary condition was imposed on the exterior surfaces of the liver and the catheter as well as a thermal insulation boundary condition. We also did not simulate the plastic enclosure holding the liver during the experiment. The simulation did not consider tissue contraction as no suitable physics-based models of thermally-induced tissue contraction were available at the time the study began.

## Experimental validation

For the experimental validation of the simulated models, a base was 3D printed (Flash Forge Creator Pro) to hold the antennas and liver as seen in Figure 9. The base was printed from Polylactic acid (PLA), the internal measurements of the base are 60 mm x 60 mm x 85 mm. The red attachment piece is 5 mm thick as the top of the liver was typically about 80 mm tall and flush with the red attachment piece (ABS) which itself was flush with the top of the base piece. The base has a 3 mm slit, for cutting the liver, in each side along the XZ plane.

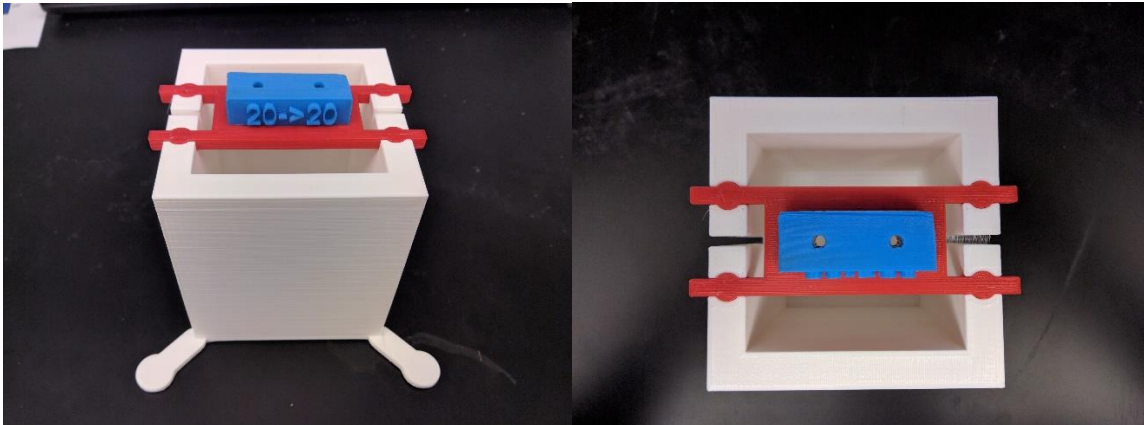


**Figure 9: Liver ablation base in white, note the slicing groove down the sides. The blue block (template block) held the antennas in position for the indicated ablation. The 20->20 figures on the template block indicates a  $D_{ins}$  distance is 20mm and a  $D_{tip}$  distance of 20mm respectively.**

The template blocks held the antennas in such a way to mimic the antenna position in the simulation. However, we did not run experiments for every single scenario that was studied in the simulations. Only four scenarios were investigated experimentally: 20 mm parallel, 20 mm to 15 mm, 15 mm parallel, and 15 mm to 10 mm.

The template blocks were printed from Acrylonitrile Butadiene Styrene (ABS) to withstand the heat from the antennas without deformation. Four template blocks were printed,

one for each of the listed scenarios. Each template block was held to the base by the red attachment plastic piece that snaps to the base to connect the base to the template blocks.

The bovine liver was procured from a local meat processing plant and cut into shape to fit the base. The pieces were warmed in a water bath (Polyscience 7306) for an hour until they reached a temperature of  $\sim 30$  °C, before the experiments started. Five experiments were ran for each scenario.

Two dipole antennas were built that operate at 2.45 GHz. These antennas are built according to the dimensions given in the paper by Curto et al [17]. The antennas were simple dipoles, with a dipole length of 10.9 mm and a gap of 1 mm. These antennas did not have any active cooling or RF choke to avoid radiation and heating along the antennas length.

For the experimental validation the antennas were fabricated using Micro coax UT-85 with a thin heat shrink tubing (3M, FP-301 26-28 AWG) acting as an insulating catheter. An SMA connector (Huber+Suhner) was attached to the end of the coax to form the connector. A Vector Network Analyzer (VNA) verified that the antennas were properly matched ( $S_{11}$  of at least -10 dB at the operating frequency) to the feeding transmission line, as seen below in Figure 10. The antennas can be seen below in Figure 11, both with and without the catheter.

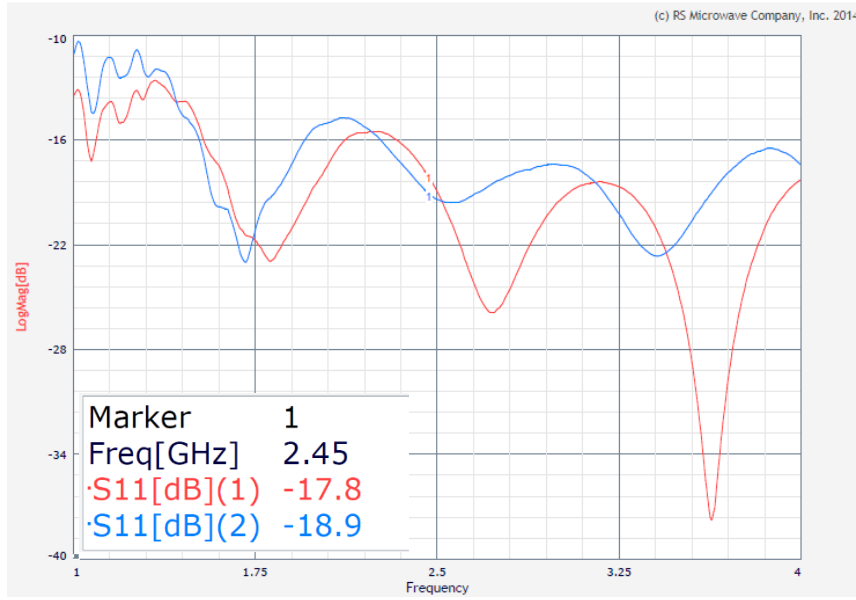


**Figure 10: S<sub>11</sub> plot from two of the dipole antennas built**

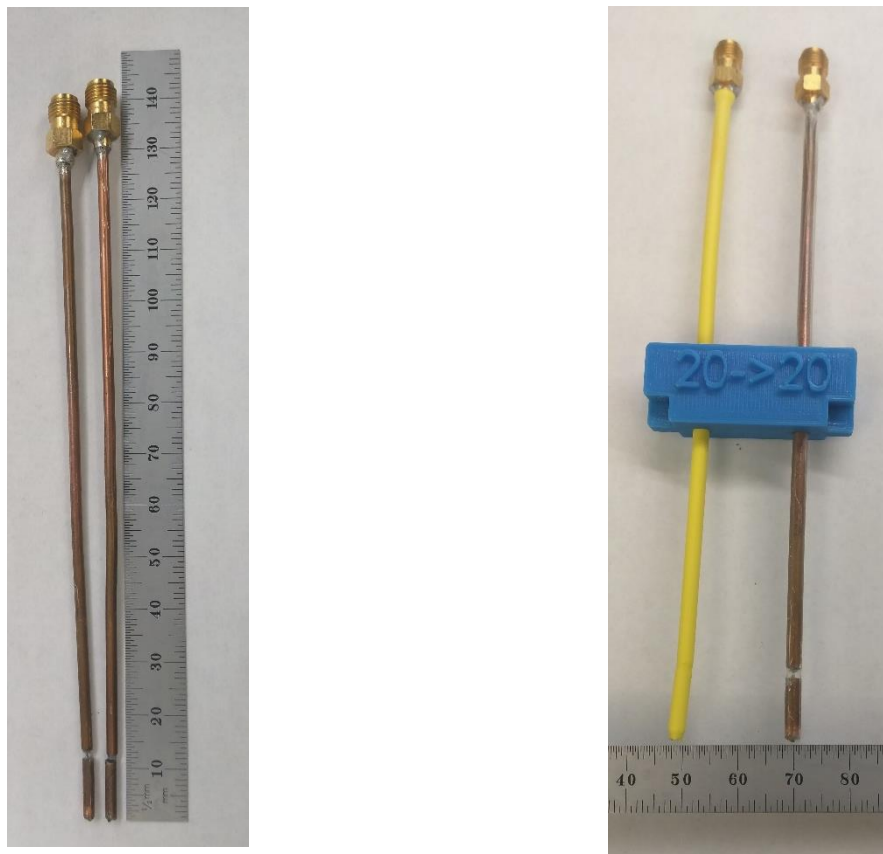


**Figure 11: Left- Antennas without the Teflon coating  
Right- Antennas with inside the template block**

For each experiment, one liver piece was removed from the water bath and placed into the base and then the template block was snapped into place. Two holes were poked into the liver, guided by the template block, with a small introducer to aid antenna insertion. The antennas were inserted 6 cm into the liver through the template block.

We generated a 30 W average forward power signal at 2.45GHz (Sairem microwave generator) and used an equal power splitter (Pasternack PE-T1000) to divide the power into two separate, phase matched signals fed to each antenna. We then used two power meters (Bird Technologies 7022-1-02020 and Bird Technologies 5012D) to track the power level from the splitter. We measured the  $S_{21}$  of the outgoing cables ( $\approx -0.12\text{dB}$ ) from the power meters into the antennas with the VNA. We adjusted the total average forward power to remain close to 30 watts. The setup is shown below in Figure 12.

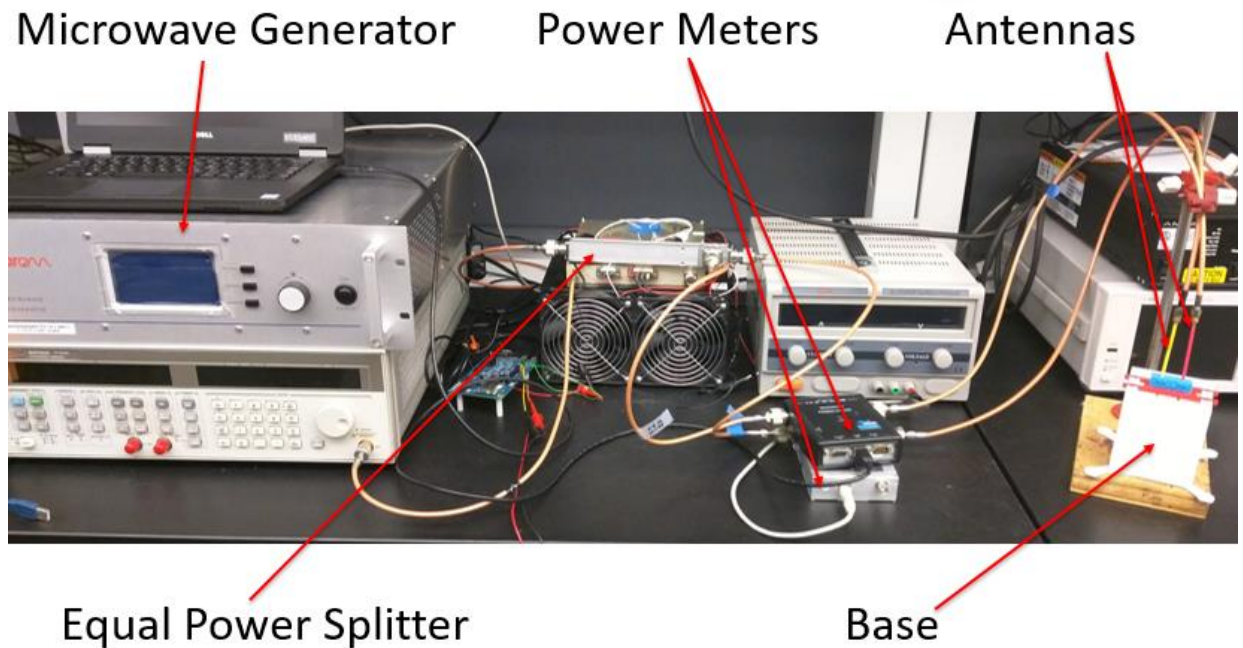


**Figure 12: Setup for experimental validation.**

After the ablation, the liver was cut in half, revealing the ablation zone in the XZ plane. This was done by removing the template block along with the red connector piece and slicing the

liver with a knife down the slot in the base shown in Figure 9. Both halves of the liver were placed on a flatbed scanner (Epson V550 photo) which was used to save a color (RGB) image of the ablation zone at 400 dpi. A scanner was used to prevent skew from photos that might appear in a hand-held photo. It has the added benefit of keeping the lighting and resolution constant for all pictures which is essential for image processing.

The resulting picture was processed in Python 3.6 with basic image processing techniques to measure the size and compare the shape of the resulting ablation zones. An example photo of the ablation zone can be seen in Figure 13.

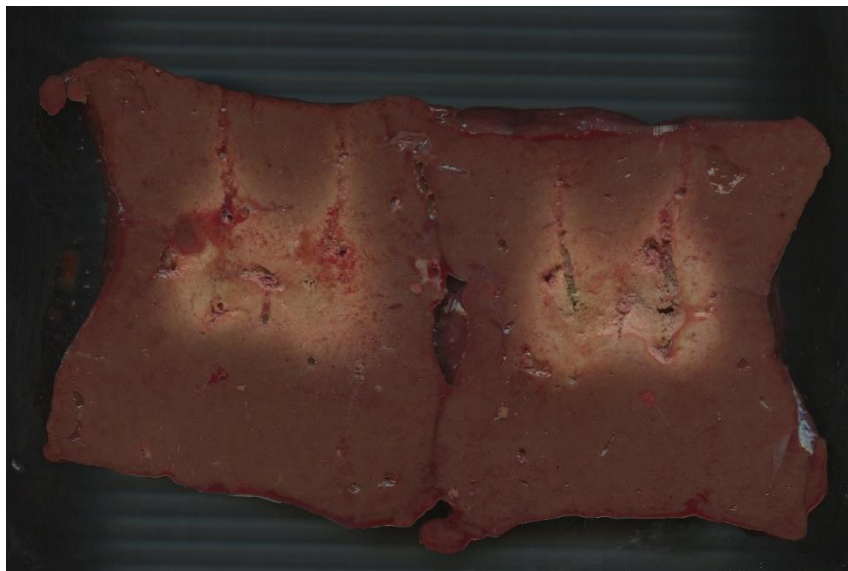


**Figure 13: Scanned Image of a 20 mm Parallel Ablation**

The image processing was done using the following modules: `numpy(1.11.3)`, `scipy(0.18.1)`, `skimage(0.14)`. The packages used for displaying images and contours were `matplotlib(2.0.0)`, `Seaborn(0.7.1)`, `matplotlib_scaelbar(0.4.1)`.

The primary method used to detect the ablated area of the liver is a basic thresh holding operation in both the RGB color space as well as the Haematoxylin-Eosin-DAB (HED) color space. We use `skimage` to convert the RGB image in to the HED color space.

The HED color space was developed in order to enable RGB cameras to detect specific immunohistochemical staining [37]. This staining of blood is used to determine aspects of the bloods composition. This deconvolution algorithm is used to facilitate the analysis of images in medicine and was also found to be useful for this application. The use of the HED color space was essential in our process, as the other color spaces lost the shape of the ablation region or allowed too much noise after thresholding.

From the original RGB image, only the red and green layers where used. The red layer threshold was set at 110 and green layer threshold was set at 75 out of the possible 255 levels. For the HED color space, only the first layer was the middle Eosin layer of the HED color space at 0.34. These were chosen based on a trial and error basis by qualitative comparison to the original photo. The color space plots after thresh-holding are seen below in Figure 14. The combined color maps can be seen in the bottom right corner after a binary OR of the three thresholded pictures.

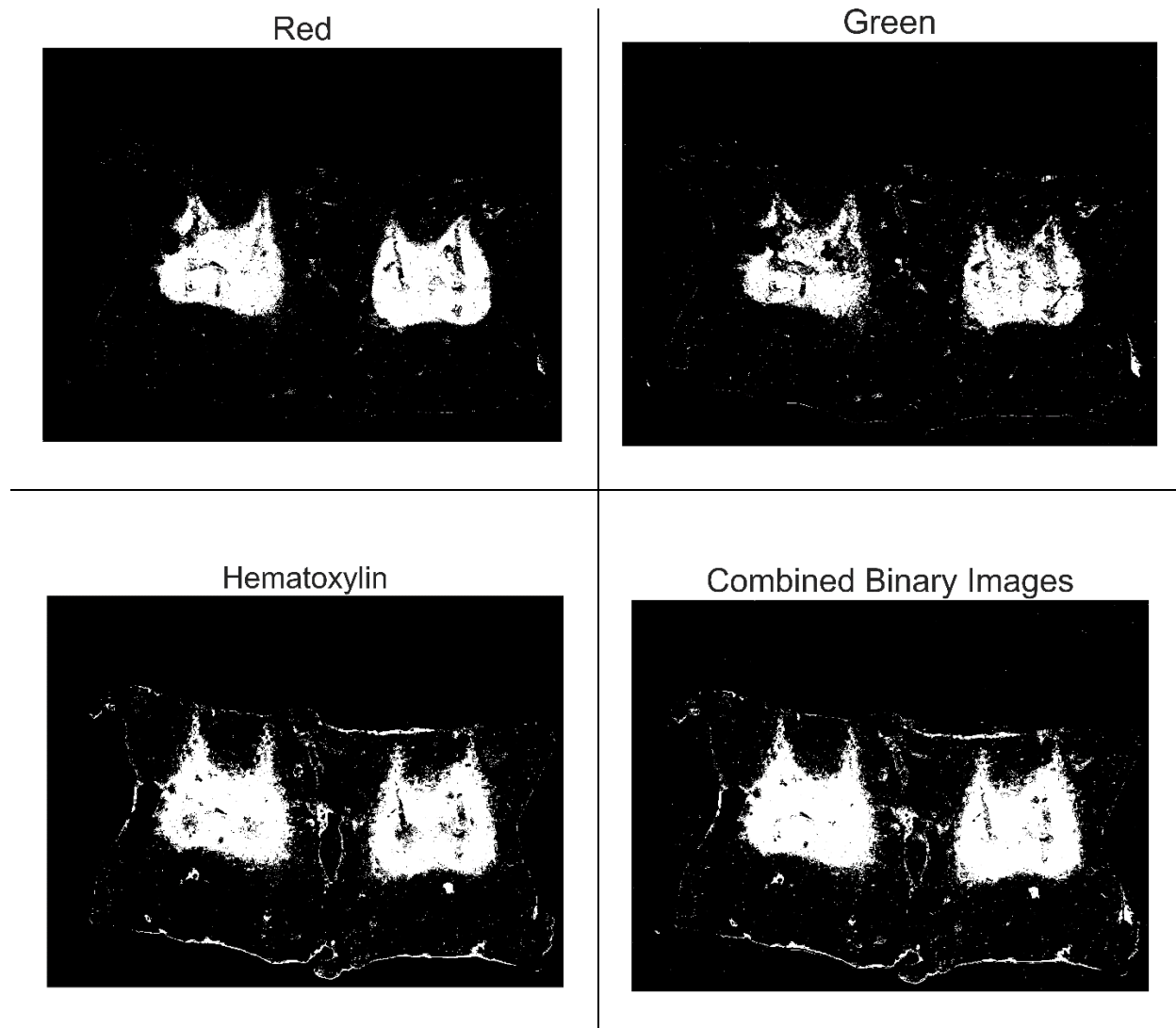


**Figure 14: Color spaces used in ablation detection after threshold.**

Then scipy was used to perform a small Gaussian blur( $\sigma = .19$ ) on the resulting non-binary image to remove noise in the image as seen in Figure 15 and then converted back to a binary image. After that a series of morphological operators (erosion, then dilation using a disk of size 3 pixels) further reduced noise and smoothed the edges of the ablation zone seen in Figure 16.

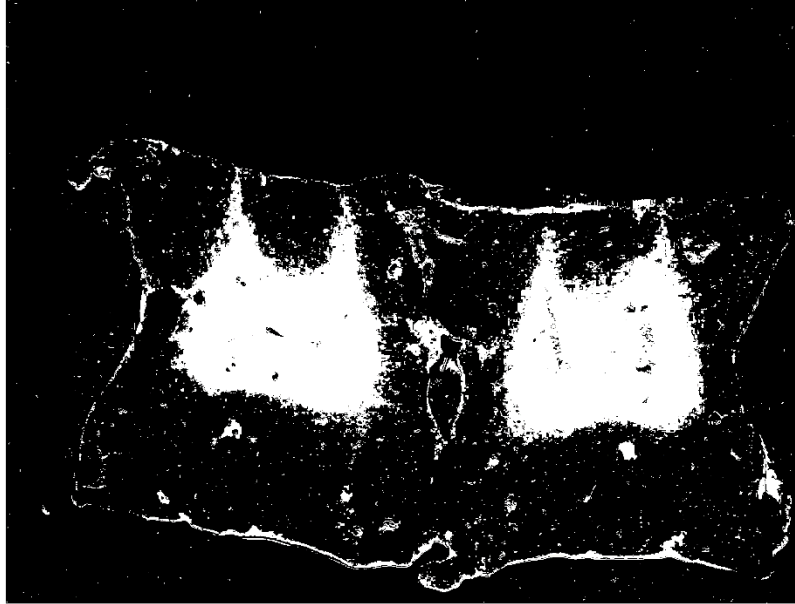


**Figure 15: Combined color spaced image with Gaussian blur applied**

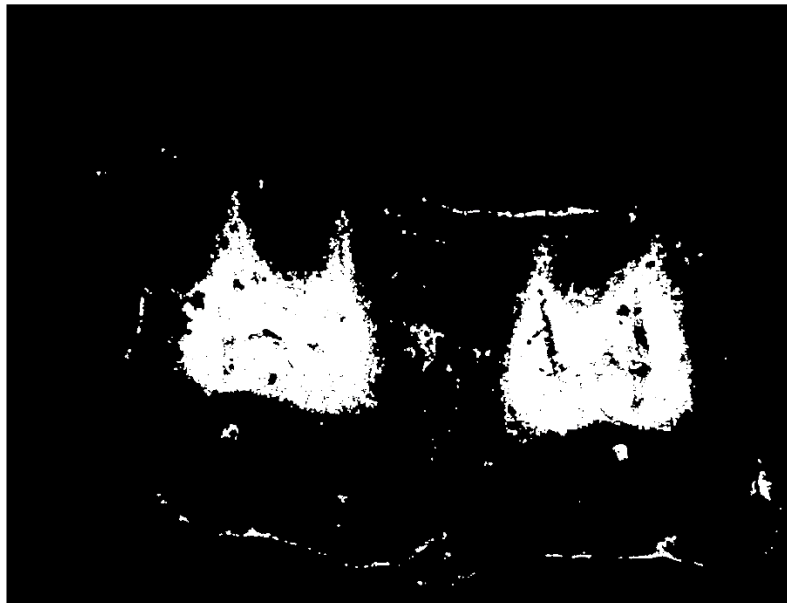


**Figure 16: Image after morphological operators.**

After the morphological operators, a scipy function, binary fill holes, was used to fill in the holes in the middle of the ablated region. The result is below in Figure 17. Since most of the noise has been removed from in the image, skimage region properties was used to single out the region

we would like to keep. The ablation region was the largest region in the image after the nose removal. After finding the largest area, we used an edge detection on that area to determine the size of the ablation zone. The largest area is seen in Figure 18. The edge from Figure 18 is overlaid on the original image (Figure 13) for a visual comparison. This is as shown in Figure 19.

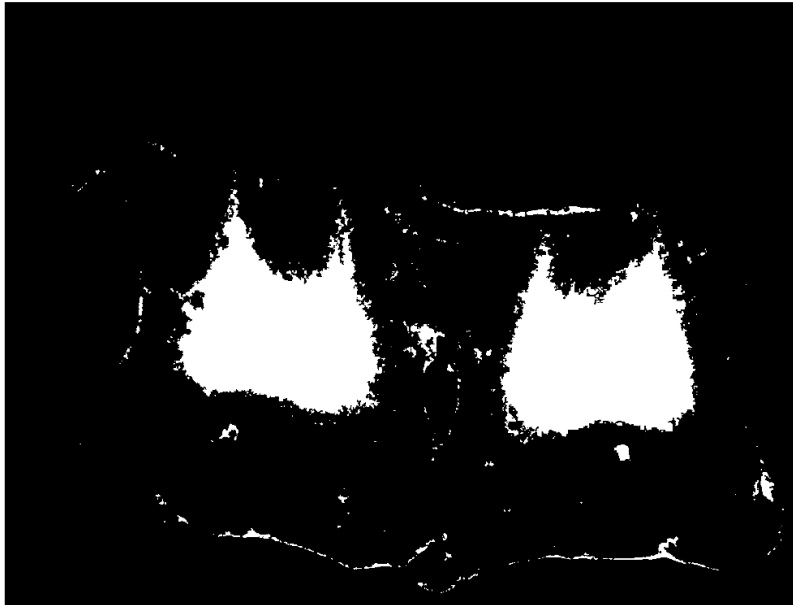


**Figure 17: All holes filled**

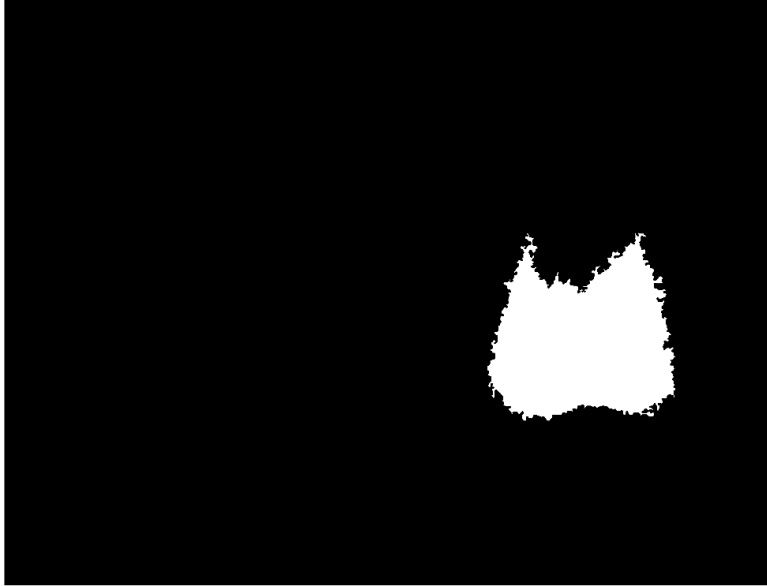


**Figure 18: Largest area in picture**



**Figure 19: Outline of ablation Area**

Once the shape of the shape of the ablation region has been found, for all the ablations for a given scenario, they are compiled together. To compile the ablation outlines, they were moved to the center of the image and in the same orientation.

Region properties of the ablation zone were used to find the center of mass for each ablation area. The detected center of mass for our example is seen below in Figure 20. We also applied a rotation on an image by image basis depending on the placement of the liver on the scanner bed. The angle of rotation was determined qualitatively for each of the ablation areas.

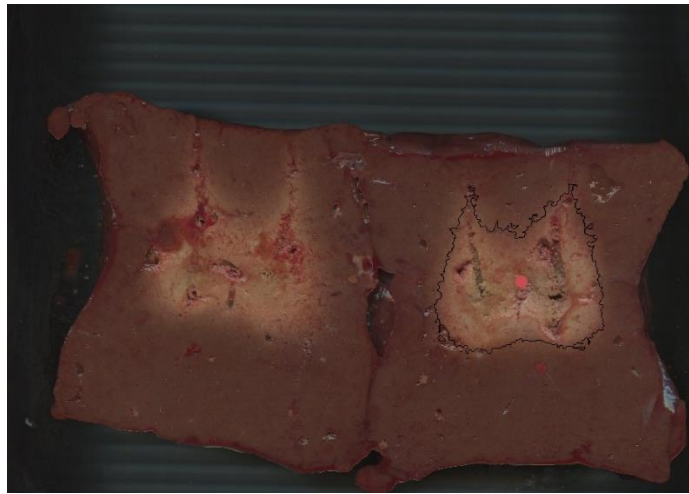


**Figure 20: Ablation with the centroid shown at the pink dot.**

After we had aligned the ablation shapes, we added the binary score (0 or 1) for each pixel from multiple repetitions of each ablation scenario together to find the composite ablation image. Since we performed  $n = 5$  experiments for each experimental scenario, this composite image contained only integers with values that ranged between zero and five. This image can be seen in Figure 21.

The values of five occurred in regions where the tissue was ablated in each of the five experiments; likewise, the areas that had a value of one are locations where the tissue was ablated in only one of the five experiments. The darkest mass in the center was the area that all experiments ablated. From this, we found the maximum and minimum ablation shape for each scenario, as well as the 75% contour ablation shape (the shape that we would expect to see ablated in 75% of ablations). To find the maximum, we convert the image to a binary image where only

the highest number (5) would be a one, all else would be zero. After that, a canny edge detection was used to find that shape.



**Figure 21: Aligned and Rotated Ablation Shapes for 20mm Parallel Ablation (colors are inverted, 0 is white)**

### **Area comparison with Dice Similarity Coefficient (DSC)**

We compared the shape of the ablation zone extents from experiments using the Dice Similarity Coefficient (DSC) metric. This is a commonly used metric in image processing applications to compare shape similarity. The equation for the DSC calculation can be seen in Equation 6.

$$\text{DSC} = \frac{2 |A \cap B|}{|A| + |B|} \quad (6)$$

For the experiments, A and B are binary images that have been detected through image processing. Specifically, the areas inside some contours (typically the 75% contour). For

simulations we use the XZ plane that bisects the liver and antennas and considered only points on that plane that are at or above 55°C as our ablation zone. We also employed a volumetric approach and considered the entire volume of the ablation that is above 55 °C to compare extents of the ablation zone in 3D for the simulations.

## Chapter 3 - Results

### Experimental

Overlaying ablation regions from multiple ablation experiments was the primary source of data for our experimental results. As discussed above, these superimposed images showing the ablation area allow us to remove experimental error by allowing us to find what a “typical” shape might be for a given scenario. Another benefit is that a comparison of complex ablation scenarios can be made by analyzing the shape of the ablation zones. The results from the experiments are shown in Figure 22. This figure shows the minimum and maximum ablation area for each scenario. The inner most line represents the edge of the ablation zone that was found in all five experiments for the given scenario. The outer most line represent the absolute farthest extent of any ablation.

We also found the 75% ablation contour, the shape that was ablated by 75% of experiments, shown in Figure 23. Figure 24 shows the overlay of the 75% contour. This figure is comparing the parallel (20 mm parallel) and non-parallel (20 mm to 15 mm). This is demonstrating the difference in ablation cross section one might see given a non-parallel insertion of ablation antennas, compared to a parallel insertion.

When comparing the measured area for each ablation in each scenario, the DSC was used. The area of each parallel ablation to the area of each non-parallel ablation for the same given antenna spacing. As five experiments where completed for each scenario, there were 25 comparisons to make for 20 mm spacing, and 25 for the 15 mm spacing. The DSC results of our experiments are shown in Table 5.

Antenna spacing	15 mm	20 mm
Mean	0.805	0.733
Standard Deviation	0.0036	0.0575
Variance	0.06	0.0033

**Table 5: Table showing the DSC of the experimental ablation zone for antennas inserted in the parallel case compared to the non-parallel case.**

 Area ablated by all five experiments

 Area ablated from any combination of experiments

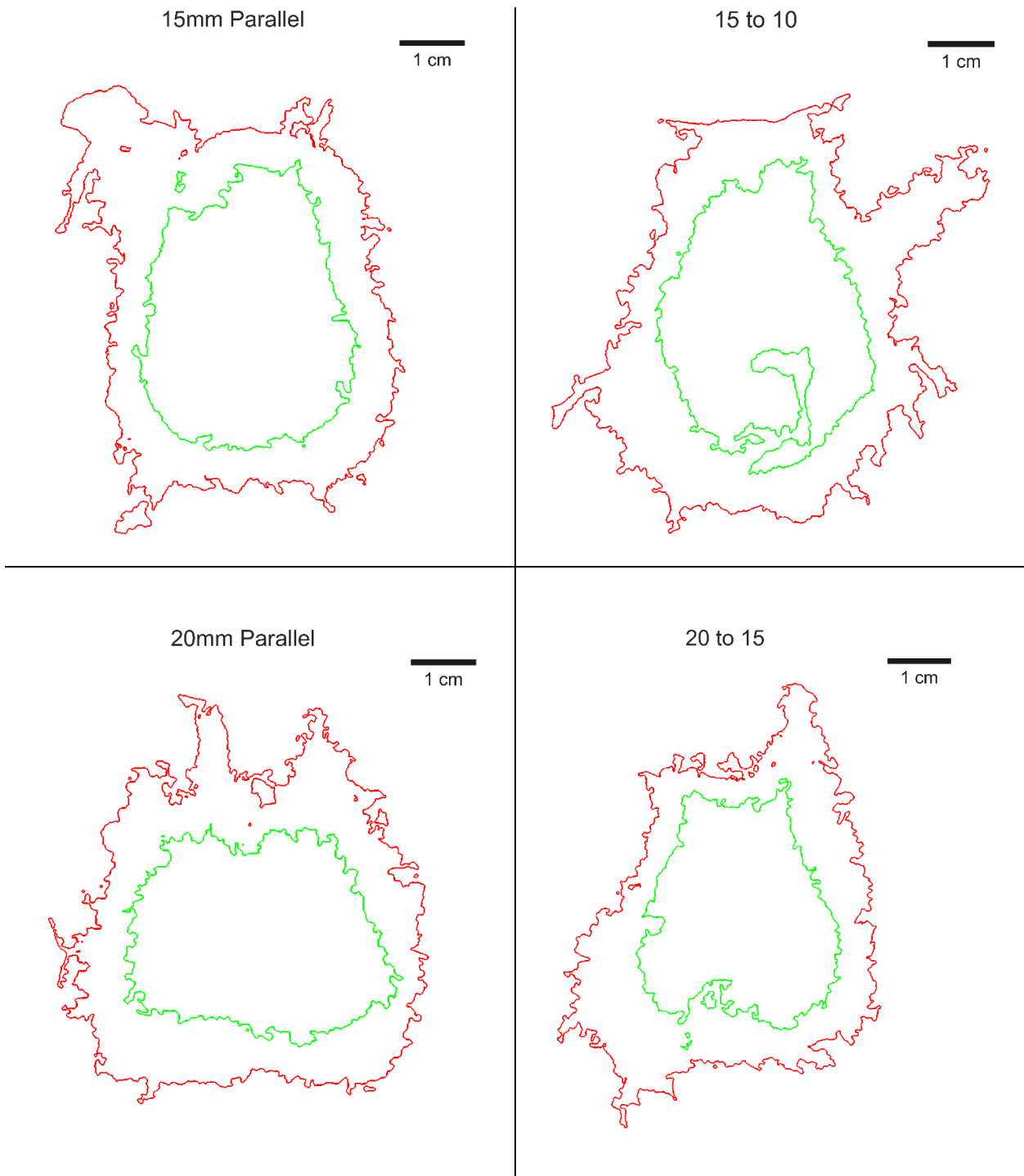
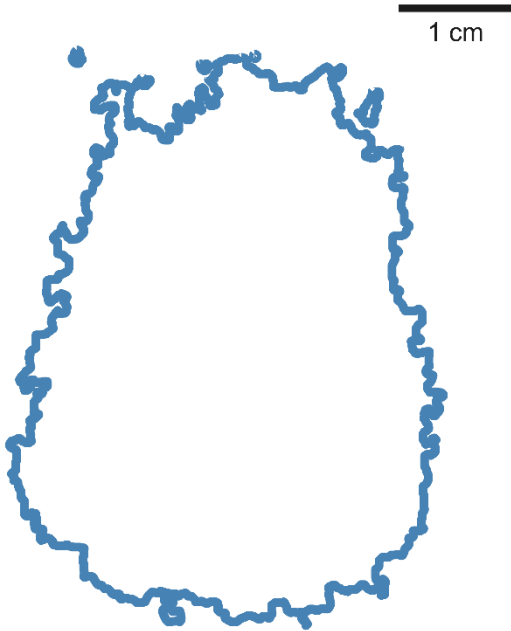
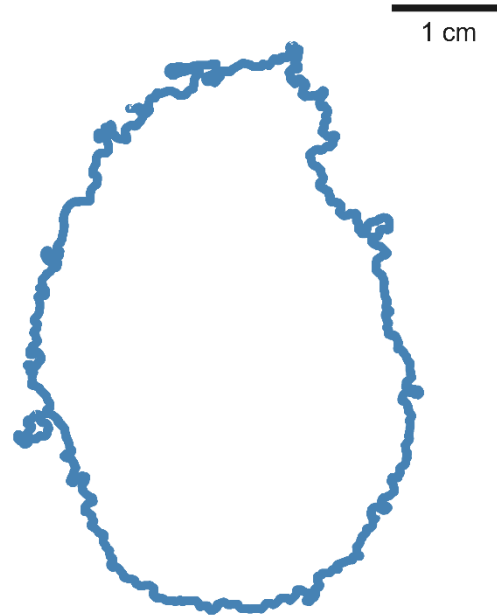


**Figure 22: Ablations all resulted in a shape in between the shown red and green lines for a given scenario. Lines that are close together imply a smaller uncertainty for that ablation zone.**

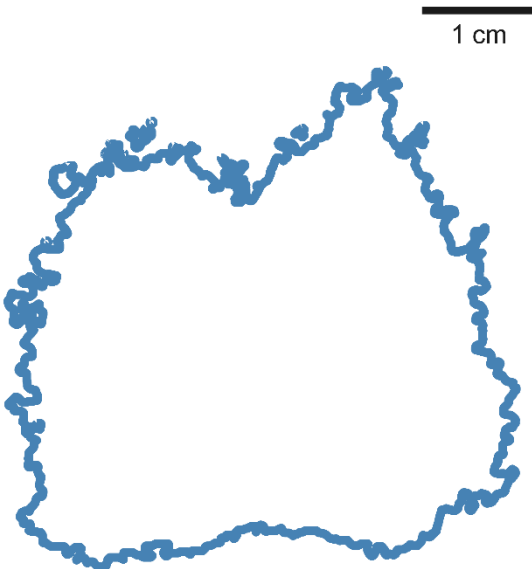
15mm Parallel 75% Ablation



15mm to 10mm 75% Ablation



20mm Parallel 75% Ablation



20mm to 15mm 75% Ablation

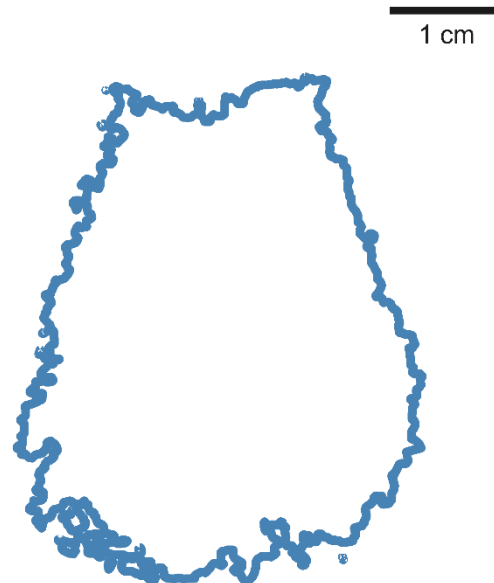


**Figure 23: 75% contours of ablations for each scenario. This is what a typical ablation might look like for the antenna spacing, insertion angle, and power.**

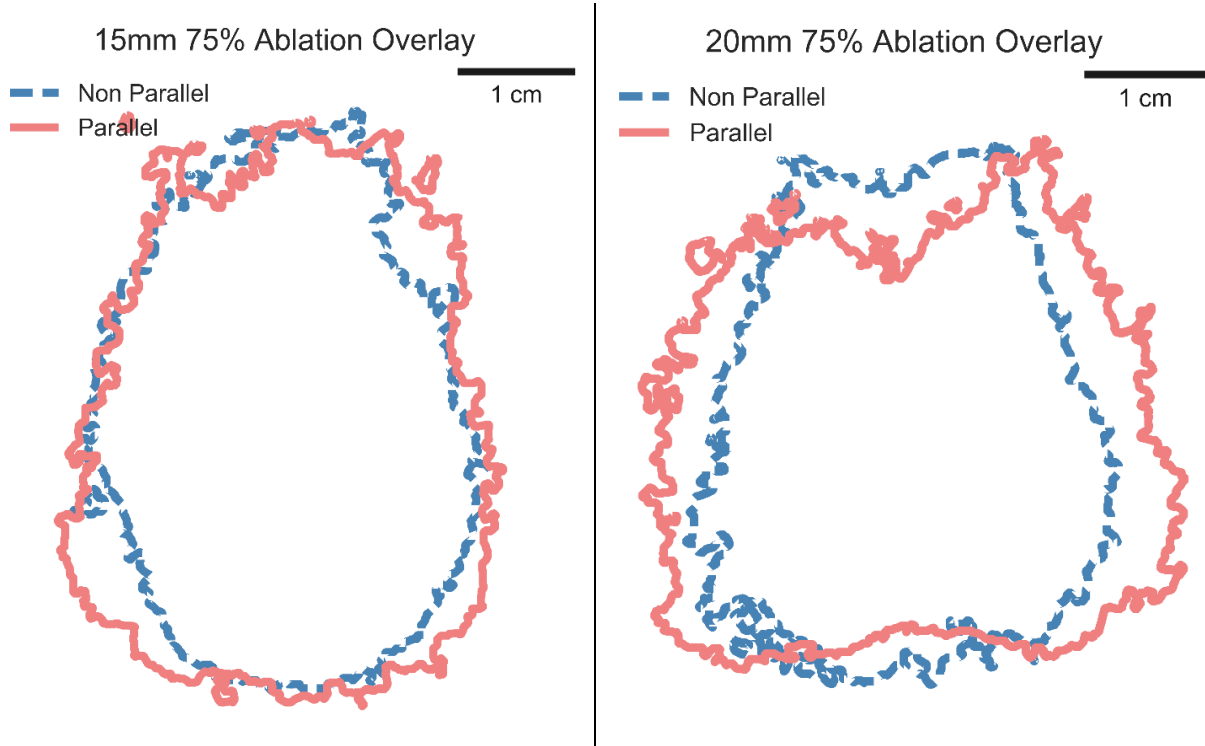


**Figure 24: Area of ablation comparing parallel to on parallel in experimentation. The contours shown are the 75% confidence contours.**

## Simulation

As stated previously, the 55 °C isothermal contour in the simulation was used to estimate the outer edge of the simulation ablation area. For now, only the four simulated ablation scenarios that were also tested in the experimentally are going to be considered. The results of all four scenarios can be seen below in Figure 25 in the XZ plane.

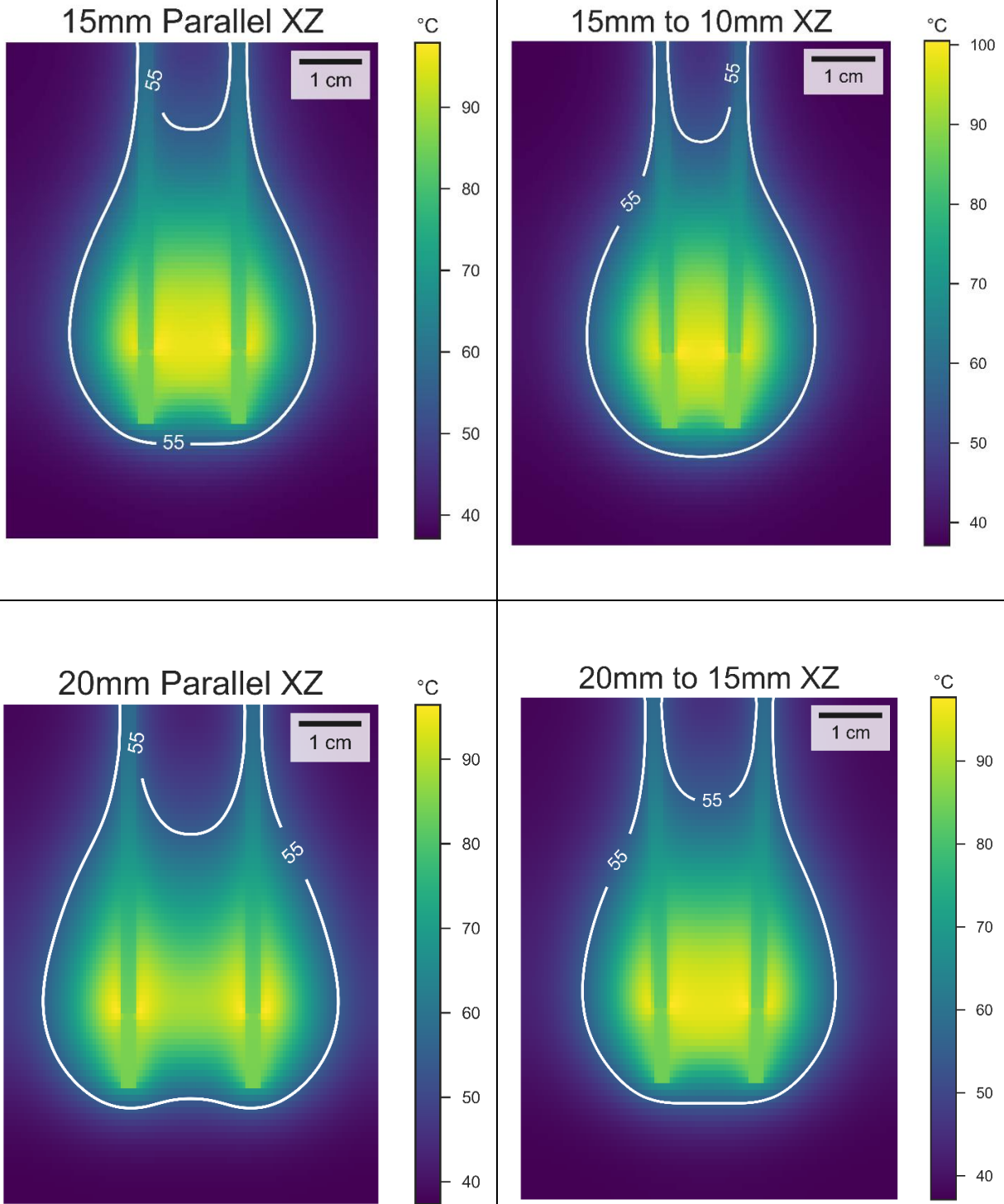


**Figure 25: Simulation 55 °C XZ isothermal contours.**

If we view the same simulation results along the YZ Axes we can see how wide that ablation zone is at the midline. This can be seen below in Figure 26.

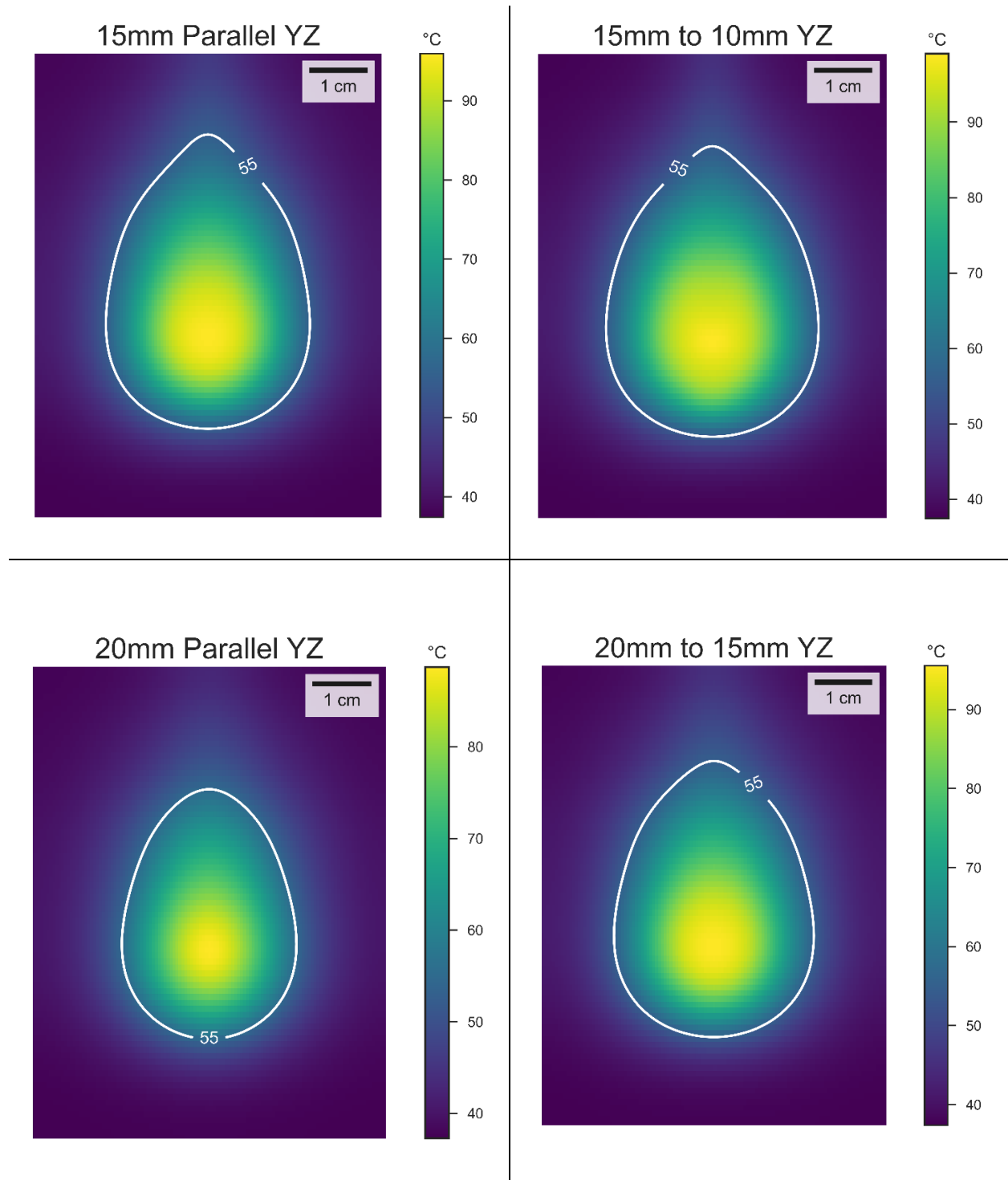


**Figure 26: Simulation 55 °C YZ isothermal contours**

Finally, the ablation area shape as cut symmetrically between the two antennas, in the XY plane are shown in Figure 27.

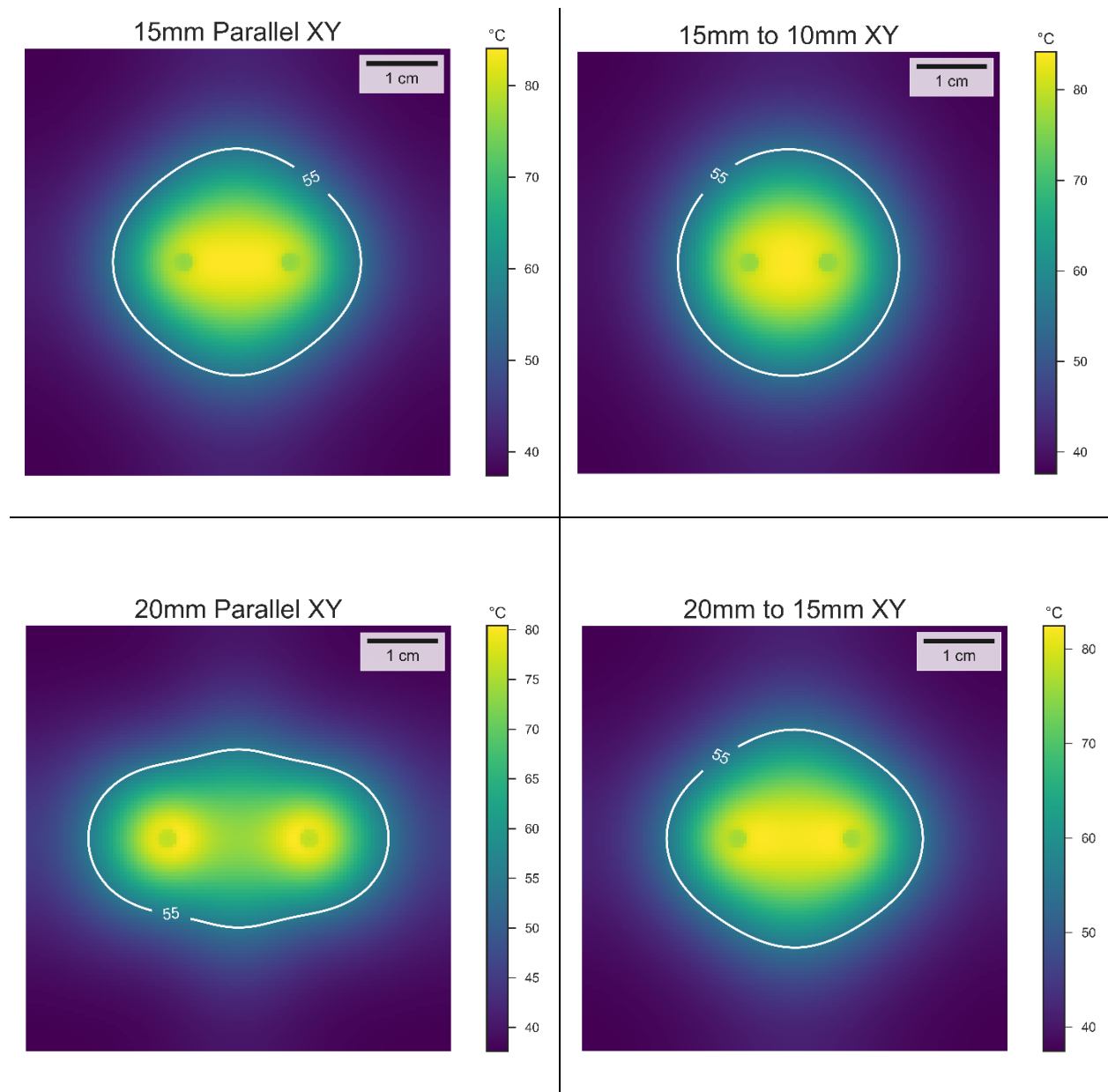


**Figure 27: Simulation 55 °C XY isothermal contours**

Further comparisons between the parallel and nonparallel cases can be made by overlaying the isocontours from the XZ slices from Figure 25 as shown in Figure 28.

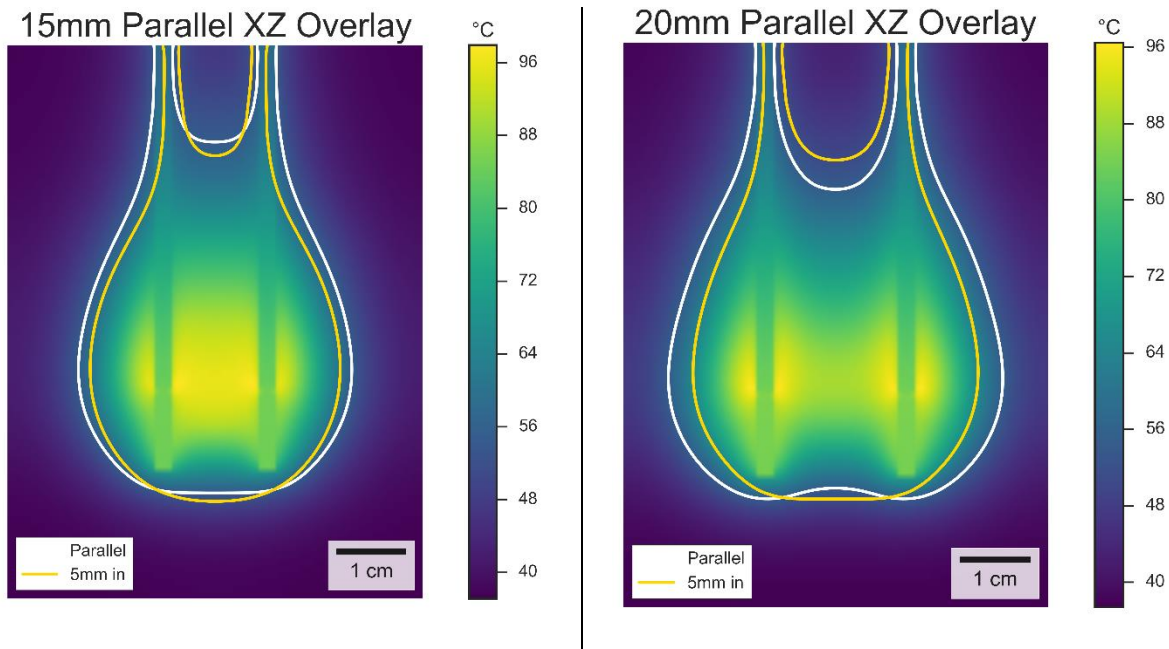


**Figure 28: Overlaid 55°C isothermal outline of parallel and non-parallel cases**

The Dice-similarity Coefficient was used to compare the area of the parallel and nonparallel cases, as shown in Table 6.

### **Extended Simulated Results**

In the last section we examined the results of both experiment results and simulated results to establish that there is a connection between the simulation and experimentation. The setups examined were: 15 mm parallel, 15 mm to 10 mm, 20 mm parallel, and 20 mm to 10 mm. There are also simulated results for a larger set of scenarios than just the ones mentioned above. These other scenarios are the anticipated ablation zones for an ablation for a more extreme case than previously examined in the experimental validation. For these purely simulated scenarios, we are considering the volumetric DSC as opposed to a planar DSC to show the change of the ablation volume. The results are shown below in Table 7, Table 8, and Table 9.

Antenna spacing	15 mm	20 mm
DSC	.92	.85

**Table 6: DSC of simulation comparing ablation area of the parallel case to the corresponding non-parallel case (i.e. 15mm to 15->10) in the XZ plane.**

	20 mm Parallel	20 mm to 15 mm	20 mm to 10 mm	20 mm to 5 mm
20 mm Parallel	1.0			
20 mm to 15 mm	.845	1.0		
20 mm to 10 mm	.776	.919	1.0	
20 mm to 5 mm	.718	.714	.728	1.0

**Table 7: Volumetric DSC for simulations with 20 mm antenna spacing**

	15 mm Parallel	15 mm to 10 mm	15 mm to 5 mm
15 mm Parallel	1.0		
15 mm to 10 mm	.927	1.0	
15 mm to 5 mm	.89	.95	1.0

**Table 8: Volumetric DSC for simulations with 15 mm antenna spacing**

	10 mm Parallel	10 mm to 5 mm
10 mm Parallel	1	
10 mm to 5 mm	.947	1

**Table 9: Volumetric DSC for simulations with 10 mm antenna spacing**

## Chapter 4 - Discussion

While it is known that that using multiple microwave ablation antennas generally creates a larger ablation zone than a single antenna supplied with the same total forward power, it is not yet understood how that zone changes for non-parallel insertion. The goal of this study was to determine the impact of non-parallel insertion for multiple antenna microwave ablation. We used a 3D FEM simulation and performed experimental ablations in *ex vivo* bovine liver for this investigation.

Experimental results show that there is a larger difference for non-parallel insertion for a wide antenna spacing as compared to a narrower antenna spacing as seen in Table 5. This is consistent with Figure 24 which shows that the 20 mm spacing ablation zone varies much more when non-parallel as compared to the 15 mm spacing.

The simulated results in Figure 28 show that the simulations predicted similar trends in size and shape of the ablation zone as observed in experiment. In this figure it is also clear that the wider antenna spacing does significantly impact the ablation zone, as it was in Figure 24. This is further shown by comparing Table 5 and Table 6 which show that for both experiments and simulation, the wider antenna spacing results in greater than 7% change in similarity. A reason that the absolute values of Table 5 and Table 6 do not match may be due to the fact that we did not include the effects of tissue contraction in our simulations. When comparing Figure 23 and Figure 25 we see that the predicted ablation shape dimensions align well with the actual measured ablation shape.

Finally the DSC comparing volumes of simulated ablation zones for parallel and non-parallel cases is shown in Table 7, Table 8, and Table 9. These data show a similar trend to the planar DSC values presented in Tables 5 and 6. For non-parallel insertion, the closer together the

antenna spacing is, the more similar the resulting ablation zone will be to a parallel insertion. In this case, if the antenna tips are 5 mm closer together, the 10 mm spacing is about 5% different, while the 20 mm spacing is about 15% different than the parallel case. Table 7 also suggests that there may be a notable change from the nominal ablation shape as the antennas tend toward being much less parallel. We see that the 20 mm parallel ablation zone compared to the 20 mm to 5 mm non-parallel configuration has a 30% difference.

## Chapter 5 - Conclusion

The use of microwave ablation for treating HCC is becoming more commonplace, especially for those patients that are ineligible for surgery. Clinicians who deploy multiple antennas for treating HCC sometime may not always be able to insert the antennas parallel to each other, and it is not yet known what impact this has on the ablation outcome. This thesis was an investigation to assess what the change in ablation volume might be for a non-parallel insertion. These results may serve as a guide to practitioners to determine the potential impact of non-parallel antenna insertion when conducting clinical procedures.

We found that nonparallel insertion could have a measurable change on the ablation size and volume for our setup. There was up to a 30% variability for some of the more severe cases of nonparallel insertion that we studied. We also found that the rate of change for ablation size does vary considerably and did not vary linearly with the distance of the tip displacement from the original parallel position.

The model we used for simulating our ablation was relatively accurate at predicting the shape of the ablation for our experiment and was also capable of showing how the ablation shape would change given for a small tip offset distance. The amount of similarity between the parallel and non-parallel insertions did vary when comparing the simulation and the experimentation, possibly due to unaccounted tissue shrinkage in the simulations.

## References

- [1] M. F. Meloni *et al.*, “Microwave ablation in primary and secondary liver tumours: technical and clinical approaches,” *Int. J. Hyperthermia*, vol. 33, no. 1, pp. 15–24, Jan. 2017.
- [2] R. L. Siegel, K. D. Miller, and A. Jemal, “Cancer statistics, 2017,” *CA. Cancer J. Clin.*, vol. 67, no. 1, pp. 7–30, Jan. 2017.
- [3] M. Li, X. Yu, P. Liang, F. Liu, B. Dong, and P. Zhou, “Percutaneous microwave ablation for liver cancer adjacent to the diaphragm,” *Int. J. Hyperthermia*, vol. 28, no. 3, pp. 218–226, May 2012.
- [4] K. Okuda, H. Obata, Y. Nakajima, T. Ohtsuki, N. Okazaki, and K. Ohnishi, “Prognosis of Primary Hepatocellular Carcinoma,” *Hepatology*, vol. 4, no. S1, p. 3S–6S, Jan. 1984.
- [5] L. S. Poulou, “Percutaneous microwave ablation vs radiofrequency ablation in the treatment of hepatocellular carcinoma,” *World J. Hepatol.*, vol. 7, no. 8, p. 1054, 2015.
- [6] G. Zanusi *et al.*, “Microwave Thermal Ablation for Hepatocarcinoma: Six Liver Transplantation Cases,” *Transplant. Proc.*, vol. 43, no. 4, pp. 1091–1094, May 2011.
- [7] J. Dou, P. Liang, and J. Yu, “Microwave ablation for liver tumors,” *Abdom. Radiol.*, vol. 41, no. 4, pp. 650–658, Apr. 2016.
- [8] M. M. Bala, R. P. Riemsma, R. Wolff, and J. Kleijnen, “Microwave coagulation for liver metastases,” in *Cochrane Database of Systematic Reviews*, The Cochrane Collaboration, Ed. Chichester, UK: John Wiley & Sons, Ltd, 2013.
- [9] A. Andreano and C. L. Brace, “A Comparison of Direct Heating During Radiofrequency and Microwave Ablation in Ex Vivo Liver,” *Cardiovasc. Intervent. Radiol.*, vol. 36, no. 2, pp. 505–511, Apr. 2013.
- [10] J. Bruix and M. Sherman, “Management of hepatocellular carcinoma: An update,” *Hepatology*, vol. 53, no. 3, pp. 1020–1022, Mar. 2011.
- [11] K. I. Ringe, C. Lutat, C. Rieder, A. Schenk, F. Wacker, and H.-J. Raatschen, “Experimental Evaluation of the Heat Sink Effect in Hepatic Microwave Ablation,” *PLOS ONE*, vol. 10, no. 7, p. e0134301, Jul. 2015.
- [12] X. Y. Tang, Z. Wang, T. Wang, D. Cui, and B. Zhai, “Efficacy, safety and feasibility of ultrasound-guided percutaneous microwave ablation for large hepatic hemangioma: MWA for hepatic hemangioma,” *J. Dig. Dis.*, vol. 16, no. 9, pp. 525–530, Sep. 2015.
- [13] T. Schnelldorfer, A. L. Ware, R. Smoot, C. D. Schleck, W. S. Harmsen, and D. M. Nagorney, “Management of Giant Hemangioma of the Liver: Resection versus Observation,” *J. Am. Coll. Surg.*, vol. 211, no. 6, pp. 724–730, Dec. 2010.
- [14] M. Li, X. Yu, P. Liang, F. Liu, B. Dong, and P. Zhou, “Percutaneous microwave ablation for liver cancer adjacent to the diaphragm,” *Int. J. Hyperthermia*, vol. 28, no. 3, pp. 218–226, May 2012.
- [15] Y. Minami and M. Kudo, “Radiofrequency Ablation of Hepatocellular Carcinoma: A Literature Review,” *Int. J. Hepatol.*, vol. 2011, pp. 1–9, 2011.
- [16] P. Prakash, V. A. Salgaonkar, E. Clif Burdette, and C. J. Diederich, “Multiple applicator hepatic ablation with interstitial ultrasound devices: Theoretical and experimental investigation: Multiple applicator ablation with interstitial ultrasound,” *Med. Phys.*, vol. 39, no. 12, pp. 7338–7349, Nov. 2012.
- [17] S. Curto, M. Taj-Eldin, D. Fairchild, and P. Prakash, “Microwave ablation at 915 MHz vs 2.45 GHz: A theoretical and experimental investigation: Microwave ablation at 915 MHz vs 2.45 GHz,” *Med. Phys.*, vol. 42, no. 11, pp. 6152–6161, Oct. 2015.

- [18] S. Sartori, F. Di Vece, F. Ermili, and P. Tombesi, "Laser ablation of liver tumors: An ancillary technique, or an alternative to radiofrequency and microwave?," *World J. Radiol.*, vol. 9, no. 3, p. 91, 2017.
- [19] M. Ahmed, C. L. Brace, F. T. Lee, and S. N. Goldberg, "Principles of and Advances in Percutaneous Ablation," *Radiology*, vol. 258, no. 2, pp. 351–369, Feb. 2011.
- [20] C. L. Brace, "Radiofrequency and Microwave Ablation of the Liver, Lung, Kidney, and Bone: What Are the Differences?," *Curr. Probl. Diagn. Radiol.*, vol. 38, no. 3, pp. 135–143, May 2009.
- [21] D. S. K. Lu *et al.*, "Influence of large peritumoral vessels on outcome of radiofrequency ablation of liver tumors," *J. Vasc. Interv. Radiol. JVIR*, vol. 14, no. 10, pp. 1267–1274, Oct. 2003.
- [22] R. T. Groeschl *et al.*, "Recurrence after microwave ablation of liver malignancies: a single institution experience," *HPB*, vol. 15, no. 5, pp. 365–371, May 2013.
- [23] C. L. Brace, "Microwave Ablation Technology: What Every User Should Know," *Curr. Probl. Diagn. Radiol.*, vol. 38, no. 2, pp. 61–67, Mar. 2009.
- [24] M. G. Lubner, C. L. Brace, J. L. Hinshaw, and F. T. Lee, "Microwave tumor ablation: mechanism of action, clinical results, and devices," *J. Vasc. Interv. Radiol. JVIR*, vol. 21, no. 8 Suppl, pp. S192–203, Aug. 2010.
- [25] C. J. Simon, D. E. Dupuy, and W. W. Mayo-Smith, "Microwave Ablation: Principles and Applications," *RadioGraphics*, vol. 25, no. suppl\_1, pp. S69–S83, Oct. 2005.
- [26] M. S. Adams, S. J. Scott, V. A. Salgaonkar, G. Sommer, and C. J. Diederich, "Thermal therapy of pancreatic tumours using endoluminal ultrasound: Parametric and patient-specific modelling," *Int. J. Hyperthermia*, vol. 32, no. 2, pp. 97–111, Feb. 2016.
- [27] T. Ishizawa *et al.*, "Surgical technique: new advances for expanding indications and increasing safety in liver resection for HCC: The Eastern perspective," *J. Hepato-Biliary-Pancreat. Sci.*, vol. 17, no. 4, pp. 389–393, Jul. 2010.
- [28] European Association for the Study of the Liver and European Organisation for Research and Treatment of Cancer, "EASL–EORTC Clinical Practice Guidelines: Management of hepatocellular carcinoma," *J. Hepatol.*, vol. 56, no. 4, pp. 908–943, Apr. 2012.
- [29] P. Fitzmorris, M. Shoreibah, B. S. Anand, and A. K. Singal, "Management of hepatocellular carcinoma," *J. Cancer Res. Clin. Oncol.*, vol. 141, no. 5, pp. 861–876, May 2015.
- [30] T. Yin, W. Li, P. Zhao, Y. Wang, and J. Zheng, "Treatment efficacy of CT-guided percutaneous microwave ablation for primary hepatocellular carcinoma," *Clin. Radiol.*, vol. 72, no. 2, pp. 136–140, Feb. 2017.
- [31] R. C. G. Martin, C. R. Scoggins, and K. M. McMasters, "Safety and efficacy of microwave ablation of hepatic tumors: a prospective review of a 5-year experience," *Ann. Surg. Oncol.*, vol. 17, no. 1, pp. 171–178, Jan. 2010.
- [32] *Multiple Ablation Graphic*. .
- [33] "Medtronic Evident Antenna Chart."
- [34] S. Mukherjee, "Multiple Antenna Microwave Ablation: Impact of Non-Parallel Antenna Insertion," Kansas State University, 2015.
- [35] Z. Ji and C. L. Brace, "Expanded modeling of temperature-dependent dielectric properties for microwave thermal ablation," *Phys. Med. Biol.*, vol. 56, no. 16, pp. 5249–5264, Aug. 2011.
- [36] IT'IS Foundation, "Tissue Properties Database V3.0." IT'IS Foundation, 2015.

[37] A. C. Ruifrok and D. A. Johnston, "Quantification of histochemical staining by color deconvolution," *Anal. Quant. Cytol. Histol.*, vol. 23, no. 4, pp. 291–299, Aug. 2001.